ACS Macro Letters

Letter

Cite This: ACS Macro Lett. 2019, 8, 261−266

pubs.acs.org/macroletters

Creating Aligned Nanopores by Magnetic Field Processing of Block Copolymer/Homopolymer Blends

Yekaterina Rokhlenko,[†] Dimitrios Moschovas,[∥,∥] Christina Miskaki,[∥,∥] Edwin P. Chan,[§] Apostolos Avgeropoulos,[∥] and Chinedum O. Osuji*[,†,⊥]

[†]Department of Chemical and Environmental Engineering, Yale University, New Haven, Connecticut 06511, United States

[§]Materials Science and Engineering Division, National Institute of Standards and Technology, Gaithersburg, Maryland 20899, United States

[∥]Department of Materials Science and Engineering, University of Ioannina, 45110 Ioannina, Greece

[⊥]Department of Chemical and Biomolecular Engineering, University of Pennsylvania, Philadelphia, Pennsylvania 19104, United States

Supporting Information

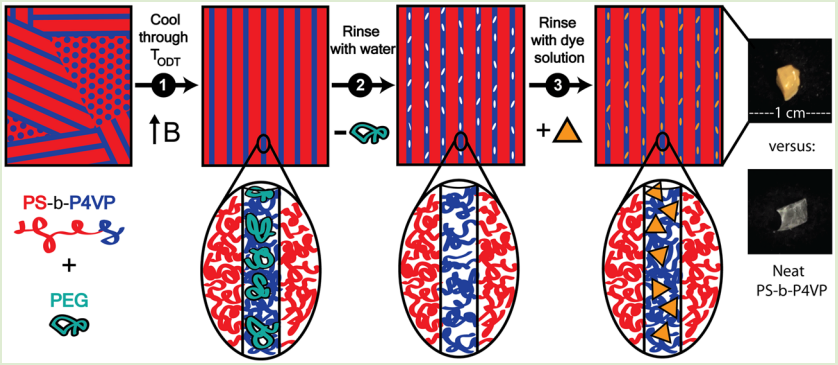

ABSTRACT: We describe the phase behavior of a cylinder-forming block copolymer (BCP)/homopolymer blend and the generation of aligned nanopores by a combination of magnetic field alignment and selective removal of the minority-block-miscible homopolymer. Alignment is achieved by cooling through the order−disorder transition temperature (T_{odt}) in a 6 T field. The system is a blend of poly(styrene-*block*-4-vinylpyridine) (PS-*b*-P4VP) and poly(ethylene glycol) (PEG). PEG is miscible with P4VP and partitions preferentially into the cylindrical microdomains. Calorimetry and X-ray scattering show that T_{odt} decreases linearly with PEG concentration until the onset of macrophase separation, inferred by PEG crystallization. Beyond this point, T_{odt} is invariant with PEG content. Increasing PEG molar mass decreases the concentration at which macrophase separation is observed. Nanopore formation is confirmed by dye uptake experiments that show a clear dependence of dye uptake on PEG content before removal. We anticipate that this strategy can be extended to other BCP/homopolymer blends to produce nanoporous materials with reliable control of pore alignment and effective pore dimensions.

Nanoporous polymers have been explored for a myriad of applications, including as membranes for separations,[1−3] for catalysis,[4] and for electrochemical systems.[5,6] They have also been explored as templates for pattern transfer[7,8] and as sensors.[9] Many of these applications require control of pore dimension, areal density, and alignment, as well as the overall mechanical and chemical properties of the material. One strategy to produce nanopores of uniform size has been to remove the cylinder-forming chains of a BCP using a selective etch process. To optimize transport in nanoporous films, it is desirable to uniformly align the nanopores along the film thickness direction. Creating vertically oriented cylinders (and, thereafter, nanopores) in thin films (≈100 nm thicknesses) can be accomplished readily by controlling interfacial interactions and by solvent vapor annealing. Apart from etching, thin films are also amenable to nanopore formation by surface reconstruction.[10] Nanoporosity can also be generated by selective homopolymer removal from BCP/homopolymer blends. The nominal size of the microdomains and the amount of homopolymer removed can be expected to provide control over the effective size of nanopores generated by this method, as shown by Jeong and Russell et al. in a PS-*b*-PMMA/PMMA system.[11] Work by Sinturel et al.[12] and Briber et al.[13] suggests that the manner of film preparation and the resulting extent of microstructure equilibration may also play a role in determining the nanoporous structure produced.

Received: January 16, 2019
Accepted: February 19, 2019
Published: February 26, 2019

DOI: 10.1021/acsmacrolett.9b00043
ACS Macro Lett. 2019, 8, 261−266

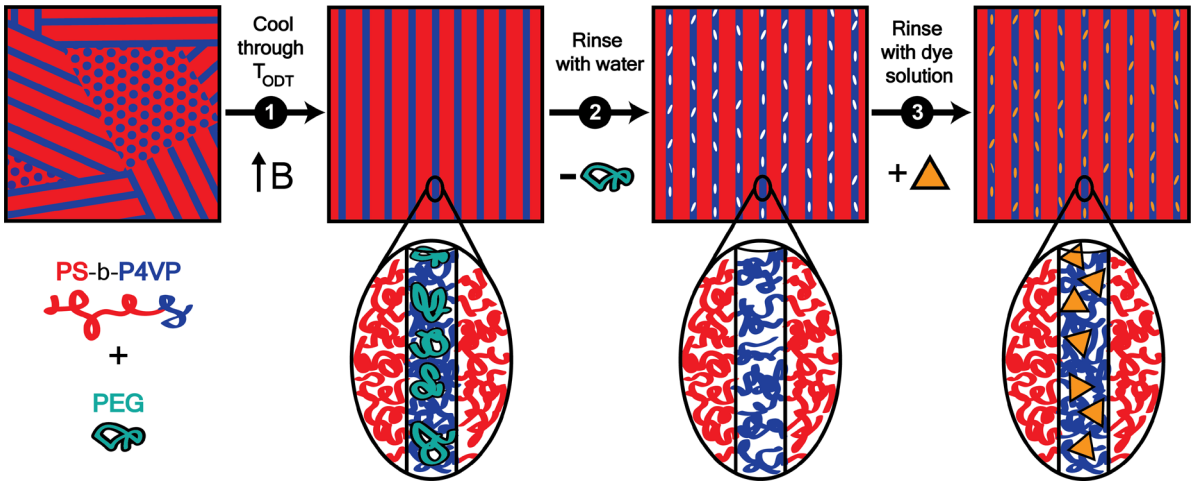

Figure 1. Illustration of strategy for forming aligned nanopores by magnetic field alignment of PS-*b*-P4VP/PEG blends. In step 1, the cylindrical microdomains formed by the P4VP/PEG mixture are aligned by cooling the material through T_{odt} in the magnetic field. In step 2, the aligned material is submerged in water to remove the PEG homopolymer. In step 3, the aligned nanoporous material absorbs dye molecules into the pores left by the PEG removal.

External forces such as shear, magnetic, or electric fields can be used for alignment of thicker films and bulk samples (≳100 nm), where surface interactions or solvent vapor annealing are ineffective in controlling microdomain orientation.[14,15] Magnetic fields have been shown to orient a variety of BCPs in the bulk, including liquid crystalline[16] and nonliquid crystalline materials.[17,18] Aligned nanopores have been produced by magnetic field processing of a liquid crystalline BCP (LC BCP) in which one block contained selectively etchable poly(lactic-acid) (PLA) side chains.[19,20] The use of self-assembly and nonsolvent-induced phase separation (SNIPS) can generate vertically aligned nanopores from block copolymers supported by an integral microporous layer.[21−23] However, the rapid phase separation and self-assembly inherent to SNIPS can result in distortion away from equilibrium structures and increased nanopore size dispersity.

Here, we combine BCP/homopolymer blending with magnetic field alignment to provide a new approach for generating polymers with aligned nanopores. As illustrated in Figure 1, a cylinder-forming BCP is blended with a sacrificial homopolymer that sequesters preferentially within the minority block. The microdomains are aligned by cooling through T_{odt} in the presence of a magnetic field. The homopolymer is removed post alignment by rinsing with a selective solvent, leaving behind aligned nanoporous cylindrical channels. The resulting nanoporous material is able to absorb dye molecules, in contrast to the neat BCP, which shows no such absorption.

The described method has several compelling aspects relative to simple etch removal of the minority block of a BCP. First, the noncovalent nature of the BCP/homopolymer association facilitates homopolymer removal and simplifies nanopore formation. Second, the effective size of nanopores created by homopolymer removal is less than can be realized by removal of the entire minority block. This has important implications given the challenge of producing sub-5 nm features in even strongly segregated BCPs.[24,25] Third, the effective pore size can be tuned by varying the amount of homopolymer in the blend. Fourth, magnetic field alignment enables the production of arbitrary microdomain orientations with no intrinsic upper limit on material thickness.

We employ this strategy with a cylinder-forming PS-*b*-P4VP BCP and PEG homopolymer, with water as the selective solvent for PEG removal. In addition to demonstrating the effectiveness of the general strategy, we investigate the effect of homopolymer molar mass and concentration on the system's structure and phase behavior using differential scanning calorimetry (DSC) and small-angle X-ray scattering (SAXS). We find that PEG addition lowers T_{odt} until the onset of macrophase separation. Beyond this point, T_{odt} becomes invariant with PEG concentration. Increasing PEG molar mass decreases the maximum loading before macrophase separation is observed.

PS-*b*-P4VP was prepared by living anionic polymerization with a total molar mass of 6.8 kg/mol (k) and P4VP mass fraction f_{P4VP} = 0.25. The system has a *d*-spacing of 11.5 nm. PEG homopolymers of three different molar masses (0.6k, 1k, 1.45k) were purchased from Sigma-Aldrich (BioUltra). The details of blend preparation are provided in Supporting Information.

DSC was used to identify relevant thermal events, including PEG crystallization and melting, and the glass transition (T_g) of PS. A clear T_g for P4VP could not be identified in any sample, likely due to its low mass fraction in the neat BCP, and possible strong T_g reduction in the blends. Figure 2 shows the DSC heating traces for neat PS-*b*-P4VP, neat PEG homopolymers, and BCP/homopolymer blends. Data on cooling are shown in Supporting Information, Figure S1. The T_g for PS is visible throughout all BCP samples at approximately 100−105 °C. The bottom panels of Figure 2a,b show the endothermic peak corresponding to the melting of PEG crystallites at 19.6, 36.9, and 48.6 °C for PEG 0.6k, 1k, and 1.45k, respectively. These values are consistent with those previously reported in the literature.[26,27] PEG is expected to be miscible with P4VP due to pyridine−hydroxyl hydrogen bonding. Increased miscibility is expected for PEG with lower molar masses in which the effect of the hydroxyl end groups are proportionately larger.[28]

PEG that has macrophase-separated from the BCP is expected to show melting peaks analogous to those of the neat PEG homopolymers. For high PEG-content blends we observe melting temperatures that are little changed relative to

DOI: 10.1021/acsmacrolett.9b00043
ACS Macro Lett. 2019, 8, 261−266

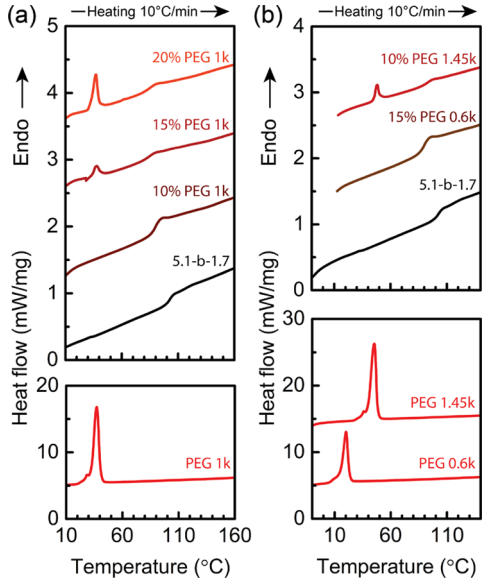

Figure 2. DSC data, with curves offset for clarity. (a) PEG 1k compared to the neat BCP, and BCP/PEG 1k blends (10%, 15%, and 20%). PEG 1k is miscible with the BCP up to 10% loading. (b) PEG 0.6k and 1.45k compared to the neat BCP, and BCP blends with 15% PEG 0.6k and 10% PEG 1.45k. PEG 0.6k remains miscible beyond 15%, while PEG 1.45k is no longer miscible, even at 10% loading, macrophase separation is evident from the PEG melting peak. The data shows that the PEG miscibility limit is inversely proportional to molar mass.

neat PEG, suggesting an absence of PEG crystallization within the P4VP microdomains. This contrasts with PS-*b*-PMMA/PEG blends in which homopolymer aggregation within PMMA microdomains resulted in crystal formation within the microdomains, but with strongly suppressed melting points.[29] Figure 2a compares DSC data of PEG 1k with the neat BCP, and PEG 1k blends (10, 15, and 20%; all compositions are in wt % of total sample mass). At 10% overall PEG content, the P4VP microdomains contain roughly 31% PEG. There are no additional peaks compared to the neat diblock, suggesting that PEG is fully incorporated as amorphous material. At 15% and 20%, a peak corresponding to PEG melting appears and grows in magnitude with increasing PEG mass fraction. Figure 2b shows comparable data to that in Figure 2a, but for two more homopolymer PEGs, one higher and one lower in molar mass than 1k. The 15% PEG 0.6k trace displays no melting peak, suggesting full incorporation of PEG with P4VP without crystallization. By contrast, the 10% PEG 1.45k trace shows a PEG 1.45k melting peak. From this data we conclude that increasing the molar mass of the PEG additive results in less sequestration of PEG by mass within the P4VP block before the onset of macrophase separation inferred by PEG crystallization.

PEG 1k was used to prepare samples for all subsequent experiments (as described in Supporting Information). Figure 3a shows SAXS profiles for the neat BCP and the BCP blended with 10% PEG 1k at 30 °C in solid black and red lines, respectively. Dotted lines of the same color show data from samples heated above their respective T_{odt} at the temperatures indicated. Both samples can be indexed to hexagonally packed cylinders. PEG addition shifts the primary scattering peak slightly toward larger q, reflecting a decrease in d-spacing from 11.5 to 11.2 nm. This modest change reflects the result of two antagonistic effects. PEG addition is expected to increase the d-spacing due to volumetric swelling. However, the presence of PEG in P4VP decreases the interaction strength between the blocks (the Flory interaction parameter at 298 K between PS and PEO, χ_{PS-PEO}[30] is almost 10× smaller than $\chi_{PS-P4VP}$[31]), leading to less chain stretching and a reduction in d-spacing ($d \sim \chi^{1/6}$ for strongly segregated systems). The net reduction in d-spacing observed on PEG addition suggests that the effect of reduced χ is significant.

SAXS data corroborate a reduction in the effective interaction strength between the BCP blocks on PEG addition. We expect PEG mixing with P4VP to affect the effective interaction parameter χ_{eff} and, thus, T_{odt}. Likewise, as PEG reaches its maximum loading with the onset of macrophase separation, T_{odt} is expected to remain constant with further PEG addition. Figure 3b shows normalized first order SAXS peak intensity versus temperature for four BCP/PEG 1k blends

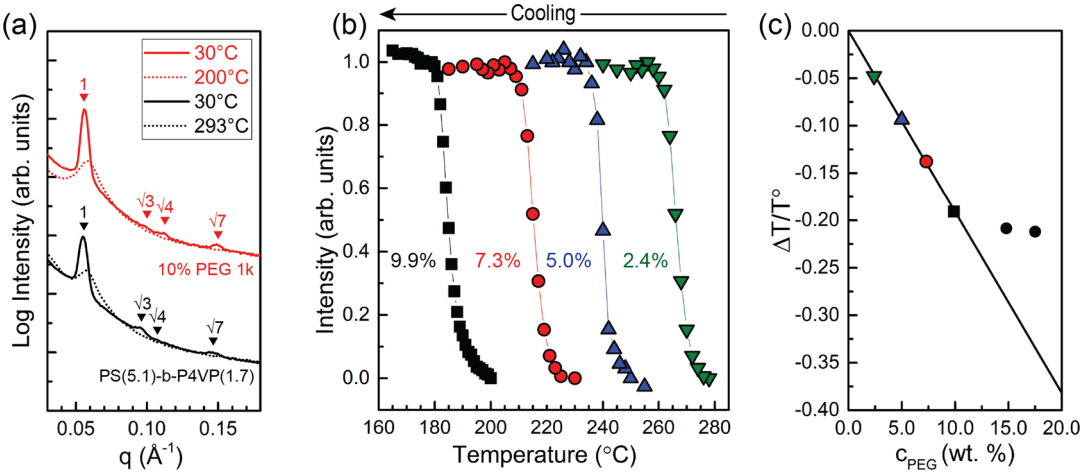

Figure 3. (a) SAXS profiles of the neat BCP and the BCP with 10% PEG 1k at 30 °C, in solid black and red lines, respectively. Dotted lines of the same color show data from the same samples heated above their T_{odt}, at 293 °C for the neat diblock and 200 °C for the 10% PEG blend. The addition of PEG drastically lowers the T_{odt} of the sample and results in a modest decrease of d-spacing from 11.5 to 11.2 nm. The curves are offset for clarity. (b) Temperature dependent intensity of primary SAXS peaks for blends with different concentrations of PEG 1k. (c) Normalized T_{odt} deviation ($\Delta T = T_{odt} - T°$) compared to the T_{odt} of the neat diblock ($T°$) plotted as a function of PEG 1k concentration (c_{PEG}).

DOI: 10.1021/acsmacrolett.9b00043
ACS Macro Lett. 2019, 8, 261−266

(2.4, 5.0, 7.3, 9.9% PEG 1k). We observe a linear reduction in T_{odt} with PEG concentration, as shown by the normalized ΔT data in Figure 3b. This reduction is consistent with a decrease in χ_{eff} on PEG addition. While the linear scaling coincides with expectations based on the dilution approximation,[32] the magnitude of the decrease in T_{odt} is noticeably larger than the dilution approximation predicts. In fact, the dilution approximation breaks down in systems with even modestly selective solvents[33−35] and, therefore, should not be expected to properly describe the strongly selective case considered here. The apparent linear scaling may be coincidental or an artifact of the limited range of concentrations considered. Two additional samples were prepared above the maximum loading of PEG, based on DSC data, at 15 and 17.5% PEG 1k. These two points (shown as black circles in Figure 3c) deviate from the linear trend observed for the four samples with PEG < 10 wt %. This observed T_{odt} plateau beyond 10% supports the conclusions made from DSC experiments that above its maximum loading, PEG begins to macrophase separate from the PS-*b*-P4VP BCP.

Samples were field aligned by cooling slowly across T_{odt} into their ordered states, in the presence of a 6 T field. Prior work estimated the magnetic anisotropy for PS-*b*-P4VP at $\Delta\chi \approx 2 \times 10^{-8}$.[17] Magnetic field alignment is thermodynamically favored when the magnetostatic free energy difference between aligned and nonaligned states $|\Delta E_m|$, exceeds thermal energy, $|\Delta E_m| = |\Delta\epsilon_m|V_g > k_BT$, where $V_g = \xi^3$ is the volume of a grain with a typical dimension ξ and $\Delta\epsilon_m = -\Delta\chi B^2/2\mu_0$, where B is the field strength and μ_0 is the permittivity of free space. In PS-*b*-P4VP, the magnetic anisotropy at the microdomain level originates from the correlation of the orientations of end−end vectors necessitated by the localization of block junctions at the microdomain interface. At a field strength of 6 T, for $\Delta\chi \approx 2 \times 10^{-8}$, grain sizes of roughly 300 nm result in a magnetostatic free energy difference similar to kT at 298 K.

With this in mind, we compared the magnetic alignment of the neat diblock to a sample of the same material, but with 10% PEG 1k added. In all cases, the cylindrical microdomains align parallel to the field. There is no discernible effect of the field on the location of the ODT, as previously observed in a lamellar PS-*b*-P4VP system.[17] Figure 4 shows the azimuthal intensity dependence $I(q = q^*,\phi)$, of the first order SAXS peak for several samples. Gaussian fits overlay the data in solid lines.

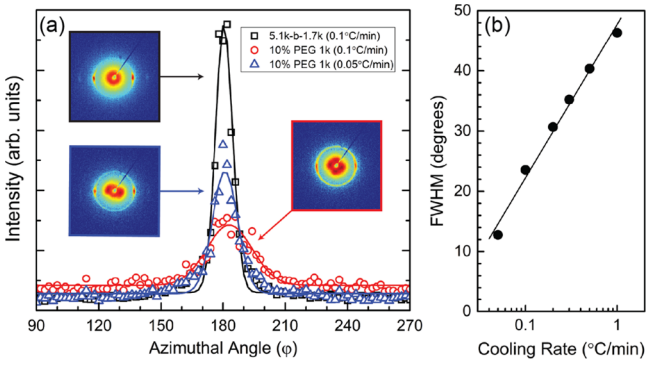

Figure 4. (a) Azimuthal intensity of neat PS-*b*-P4VP aligned at 0.1 °C/min (black squares) and 10% PEG 1k blend aligned at 0.1 and 0.05 °C/min (red circles and blue triangles, respectively). Gaussian fits are shown as solid lines. (b) Cooling rate dependent fwhm of the first order Bragg peak for the PEG-containing sample.

Insets show the 2D SAXS data. The best alignment occurs for the neat cylinder-forming BCP (shown in black) cooled 0.1 °C/min at 6 T. When 10% PEG is added, and the material is aligned at the same cooling rate and field strength (red trace), the azimuthal peak broadens and decreases in amplitude, implying a decrease in the alignment quality. We find that we can improve the alignment of the 10% PEG sample by cooling slower, at 0.05 °C/min through T_{odt} (shown in blue). Quantitative assessment of the alignment is performed by extracting the full width at half-maximum (fwhm) of the Gaussian-fitted peak shown in Figure 4a. Figure 4b shows the alignment of the 10% PEG 1k sample aligned at 6 T at varying cooling rates. The best alignment is achieved at the lowest cooling rate. The data display an apparent logarithmic dependence of fwhm on the cooling rate, suggesting that further (linear) decreases in cooling rate would bring quite limited improvements in the quality of alignment.

Figure 5 shows transmission electron microscopy (TEM) images (see Supporting Information for details) of the

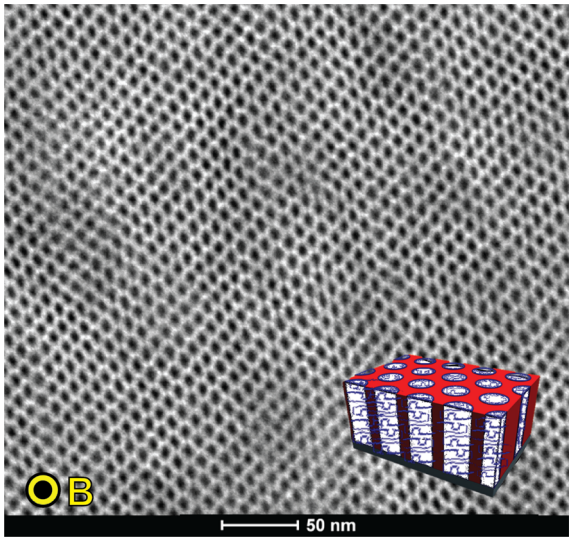

Figure 5. TEM of PS-*b*-P4VP with 10% PEG 1k aligned with a 6 T field as indicated, by cooling through T_{ODT} at 0.1 °C/min. The cylinders are aligned parallel to the field. P4VP-rich domains appear dark due to iodine vapor staining. Inset: Schematic of voids left after PEG removal in the PS-*b*-P4VP matrix.

resulting 10% PEG 1k material after alignment. The apparent square rather than hexagonal packing of the cylindrical P4VP microdomains may be due to distortion of the material during sample preparation. The inset depicts nanoporous voids left after PEG removal during sample collection from water. The absence of a clear uniform void, or voids, within the P4VP domains combined with pore diameter estimates (Supporting Information) corroborates the notion that the PEG is not concentrated at the center of the microdomains, but is distributed throughout.

Sample nanoporosity was examined by dye uptake experiments. Three samples (containing 2.5%, 5%, and 10% PEG) were aligned using the previously described protocol. Four control samples (0%, 2.5%, 5%, and 10% PEG 1k) were not aligned, but instead were thermally annealed below T_{ODT}, at 170 °C. For PEG removal, a 2−3 mg piece of each sample after either alignment or sub-T_{ODT} annealing was submerged in deionized (DI) water, then transferred to a stock dye solution,

DOI: 10.1021/acsmacrolett.9b00043
ACS Macro Lett. 2019, 8, 261−266

and finally photographed. The complete protocol is described in Supporting Information.

The results are shown in Figure 6. We find that the samples are able to absorb the dyes only if their PEG content is above a

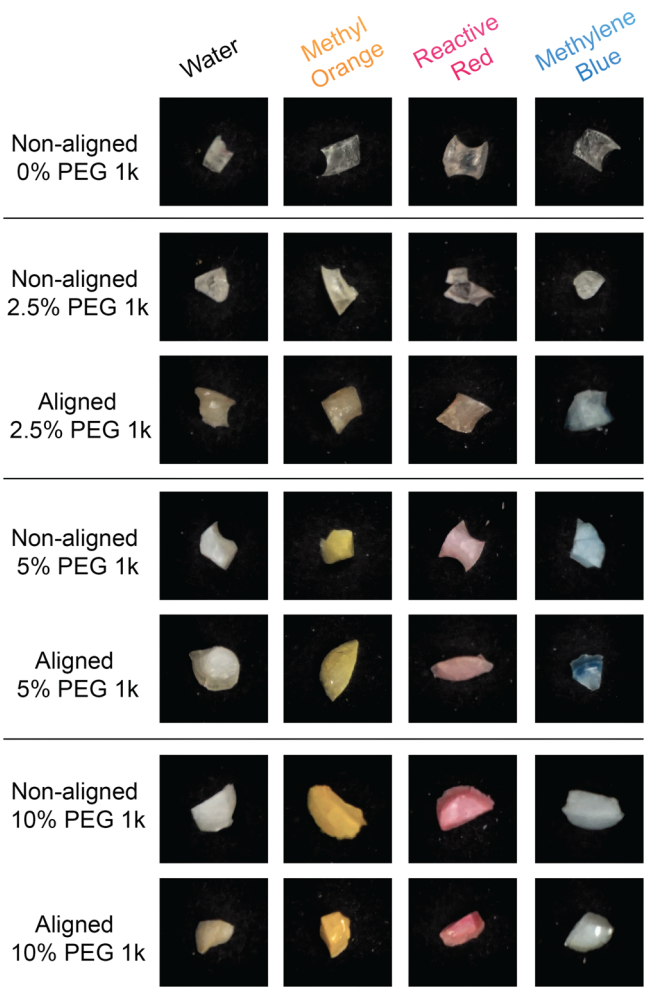

Figure 6. Results of dye absorption studies. Samples were imaged after 4 days in either water as a control or a solution of methyl orange, reactive red 120, or methylene blue. Each field of view is ≈1 cm × 1 cm.

threshold amount, roughly between 2.5% and 5%. Samples with no PEG and only 2.5% PEG showed no or only a very faint hint of color, whereas samples prepared from blends with higher PEG content were strongly colored, particularly those exposed to methyl orange and reactive red. These data suggest a correlation between the accessible pore size in the materials and the amount of PEG present in the samples before leaching. From the color intensity observed by visual inspection, the samples absorb methyl orange and reactive red more readily than methylene blue. We hypothesize that this apparent difference is due to the more effective uptake of anionic dyes (methyl orange and reactive red 120) into the basic environment of the P4VP domain, which as a basic species can be protonated to a positively charged form. The maximum loading and speed of dye uptake are likely correlated to both charge and size of dyes. The neat BCP samples (0% PEG) do not absorb dye molecules.

In summary, we have demonstrated a strategy to create nanoporous polymers with aligned channels using field-alignable BCP/homopolymer blends. Orthogonal solubility in an appropriate solvent permits selective removal of the homopolymer to generate the desired nanoporosity. We find that PEG homopolymer addition lowers T_{odt} of the PS-*b*-P4VP/PEG blend up to a maximum loading beyond which PEG macrophase separates and crystallizes. PEG loading can be used to tune the effective porosity of the system, while the PEG molar mass dictates the maximum concentration achievable before macrophase separation. Lower molar mass PEG can be incorporated to a larger extent before macrophase separation. Dye uptake experiments show that the voids produced by PEG removal are accessible for absorption, with a large increase of dye absorption visually registered for PEG concentration above 2.5%. The strategy of homopolymer inclusion and field alignment should be applicable to a broad range of polymers, permitting the creation of nanoporous materials with size-tunable nanopores.

■ ASSOCIATED CONTENT

Supporting Information

The Supporting Information is available free of charge on the ACS Publications website at DOI: 10.1021/acsmacrolett.9b00043.

DSC data and additional details on experimental protocols and sample preparation (PDF).

■ AUTHOR INFORMATION

Corresponding Author

*E-mail: cosuji@seas.upenn.edu.

ORCID

Edwin P. Chan: 0000-0003-4832-6299
Apostolos Avgeropoulos: 0000-0002-6203-9942
Chinedum O. Osuji: 0000-0003-0261-3065

Notes

The authors declare no competing financial interest.

■ ACKNOWLEDGMENTS

This work was supported by NSF (DMR-1410568). Y.R. acknowledges fellowship support from the National Physical Science Consortium (NPSC). Facilities use was supported by YINQE and NSF (DMR-1119826). The authors thank G. Doerk for assistance with DSC measurements. Certain instruments and materials are identified in this paper to adequately specify the experimental details. Such identification does not imply recommendation by the National Institute of Standards and Technology; nor does it imply that the materials are necessarily the best available for the purpose. This work is a contribution of NIST, an agency of the U.S. Government, and not subject to U.S. copyright.

■ REFERENCES

(1) Hillmyer, M. A. *Block Copolymers II*; Springer, 2005; pp 137–181.
(2) Jackson, E. A.; Hillmyer, M. A. Nanoporous Membranes Derived from Block Copolymers: From Drug Delivery to Water Filtration. *ACS Nano* **2010**, *4*, 3548–3553.
(3) Zhang, Y.; Sargent, J. L.; Boudouris, B. W.; Phillip, W. A. Nanoporous Membranes Generated from Self-Assembled Block Polymer Precursors: Quo Vadis? *J. Appl. Polym. Sci.* **2015**, *132*, na.
(4) Rose, M. Nanoporous Polymers: Bridging the Gap between Molecular and Solid Catalysts? *ChemCatChem* **2014**, *6*, 1166–1182.

DOI: 10.1021/acsmacrolett.9b00043
ACS Macro Lett. 2019, 8, 261–266

(5) Hallinan, D. T., Jr; Balsara, N. P. Polymer Electrolytes. *Annu. Rev. Mater. Res.* **2013**, *43*, 503−525.
(6) Tu, Z.; Kambe, Y.; Lu, Y.; Archer, L. A. Nanoporous Polymer-Ceramic Composite Electrolytes for Lithium Metal Batteries. *Adv. Energy Mater.* **2014**, *4*, 1300654.
(7) Park, M.; Harrison, C.; Chaikin, P. M.; Register, R. A.; Adamson, D. H. Block Copolymer Lithography: Periodic Arrays of ~ 10^{11} holes in 1 Square Centimeter. *Science* **1997**, *276*, 1401−1404.
(8) Shin, K.; Leach, K. A.; Goldbach, J. T.; Kim, D. H.; Jho, J. Y.; Tuominen, M.; Hawker, C. J.; Russell, T. P. A Simple Route to Metal Nanodots and Nanoporous Metal Films. *Nano Lett.* **2002**, *2*, 933−936.
(9) Fei, T.; Jiang, K.; Liu, S.; Zhang, T. Humidity Sensors Based on Li-loaded Nanoporous Polymers. *Sens. Actuators, B* **2014**, *190*, 523−528.
(10) Xu, T.; Stevens, J.; Villa, J.; Goldbach, J. T.; Guarini, K. W.; Black, C. T.; Hawker, C. J.; Russell, T. P. Block Copolymer Surface Reconstuction: A Reversible Route to Nanoporous Films. *Adv. Funct. Mater.* **2003**, *13*, 698−702.
(11) Jeong, U.; Kim, H.-C.; Rodriguez, R.; Tsai, I.; Stafford, C.; Kim, J.; Hawker, C.; Russell, T. Asymmetric Block Copolymers with Homopolymers: Routes to Multiple Length Scale Nanostructures. *Adv. Mater.* **2002**, *14*, 274−276.
(12) Nguyen, T.-H.; Vayer, M.; Sinturel, C. PS-b-PMMA/PLA Blends for Nanoporous Templates with Hierarchical and Tunable Pore Size. *Appl. Surf. Sci.* **2018**, *427*, 464−470.
(13) Lee, W.; Zhang, X.; Briber, R. A Simple Method for Creating Nanoporous Block-Copolymer Thin Films. *Polymer* **2010**, *51*, 2376−2382.
(14) Darling, S. Directing the Self-Assembly of Block Copolymers. *Prog. Polym. Sci.* **2007**, *32*, 1152−1204.
(15) Hu, H.; Gopinadhan, M.; Osuji, C. O. Directed Self-Assembly of Block Copolymers: A Tutorial Review of Strategies for Enabling Nanotechnology with Soft Matter. *Soft Matter* **2014**, *10*, 3867−3889.
(16) Gopinadhan, M.; Choo, Y.; Kawabata, K.; Kaufman, G.; Feng, X.; Di, X.; Rokhlenko, Y.; Mahajan, L. H.; Ndaya, D.; Kasi, R. M.; Osuji, C. O. Controlling Orientational Order in Block Copolymers Using Low-Intensity Magnetic Fields. *Proc. Natl. Acad. Sci. U. S. A.* **2017**, *114*, E9437−E9444.
(17) Rokhlenko, Y.; Gopinadhan, M.; Osuji, C. O.; Zhang, K.; O'Hern, C. S.; Larson, S. R.; Gopalan, P.; Majewski, P. W.; Yager, K. G. Magnetic Alignment of Block Copolymer Microdomains by Intrinsic Chain Anisotropy. *Phys. Rev. Lett.* **2015**, *115*, 258302.
(18) Rokhlenko, Y.; Majewski, P. W.; Larson, S. R.; Gopalan, P.; Yager, K. G.; Osuji, C. O. Implications of Grain Size Variation in Magnetic Field Alignment of Block Copolymer Blends. *ACS Macro Lett.* **2017**, *6*, 404−409.
(19) Gopinadhan, M.; Deshmukh, P.; Choo, Y.; Majewski, P. W.; Bakajin, O.; Elimelech, M.; Kasi, R. M.; Osuji, C. O. Thermally Switchable Aligned Nanopores by Magnetic-Field Directed Self-Assembly of Block Copolymers. *Adv. Mater.* **2014**, *26*, 5148−5154.
(20) Gopinadhan, M.; Choo, Y.; Mahajan, L. H.; Ndaya, D.; Kaufman, G.; Rokhlenko, Y.; Kasi, R. M.; Osuji, C. O. Directing Block Copolymer Self-Assembly with Permanent Magnets: Photopatterning Microdomain Alignment and Generating Oriented Nanopores. *Mol. Sys. Des. Eng.* **2017**, *2*, 549−559.
(21) Dorin, R. M.; Sai, H.; Wiesner, U. Hierarchically Porous Materials from Block Copolymers. *Chem. Mater.* **2014**, *26*, 339−347.
(22) Phillip, W. A.; Dorin, R. M.; Werner, J.; Hoek, E. M.; Wiesner, U.; Elimelech, M. Tuning Structure and Properties of Graded Triblock Terpolymer-Based Mesoporous and Hybrid Films. *Nano Lett.* **2011**, *11*, 2892−2900.
(23) Abetz, V. Isoporous Block Copolymer Membranes. *Macromol. Rapid Commun.* **2015**, *36*, 10−22.
(24) Sinturel, C.; Bates, F. S.; Hillmyer, M. A. High χ-Low N Block Polymers: How Far Can We Go? *ACS Macro Lett.* **2015**, *4*, 1044−1050.
(25) Azuma, K.; Sun, J.; Choo, Y.; Rokhlenko, Y.; Dwyer, J. H.; Schweitzer, B.; Hayakawa, T.; Osuji, C. O.; Gopalan, P. Self-Assembly of an Ultrahigh-χ Block Copolymer with Versatile Etch Selectivity. *Macromolecules* **2018**, *51*, 6460−6467.
(26) Pielichowski, K.; Flejtuch, K. Differential Scanning Calorimetry Studies on Poly(ethylene glycol) with Different Molecular Weights for Thermal Energy Storage Materials. *Polym. Adv. Technol.* **2002**, *13*, 690−696.
(27) *The MAK-Collection for Occupational Health and Safety*; American Cancer Society, 2012; pp 248−270.
(28) Barton, A. F. M. *Handbook of Poylmer-Liquid Interaction Parameters and Solubility Parameters*; Routledge, 1990.
(29) Chen, N.; Yan, L.-T.; Xie, X.-M. Interplay between Crystallization and Phase Separation in PS-b-PMMA/PEO Blends: The Effect of Confinement. *Macromolecules* **2013**, *46*, 3544−3553.
(30) Frielinghaus, H.; Mortensen, K.; Almdal, K. Differences of Interaction Parameter of a PS/PEO homopolymer blend and diblock copolymer in comparison to other systems. *Macromol. Symp.* **2000**, *149*, 63−68.
(31) Zha, W.; Han, C. D.; Lee, D. H.; Han, S. H.; Kim, J. K.; Kang, J. H.; Park, C. Origin of the Difference in Order- Disorder Transition Temperature between Polystyrene-block-poly (2-vinylpyridine) and Polystyrene-block-poly (4-vinylpyridine) Copolymers. *Macromolecules* **2007**, *40*, 2109−2119.
(32) Helfand, E.; Tagami, Y. Theory of the Interface between Immiscible Polymers. II. *J. Chem. Phys.* **1972**, *56*, 3592−3601.
(33) Lodge, T. P.; Pan, C.; Jin, X.; Liu, Z.; Zhao, J.; Maurer, W. W.; Bates, F. S. Failure of the Dilution Approximation in Block Copolymer Solutions. *J. Polym. Sci., Part B: Polym. Phys.* **1995**, *33*, 2289−2293.
(34) Hanley, K. J.; Lodge, T. P.; Huang, C.-I. Phase Behavior of a Block Copolymer in Solvents of Varying Selectivity. *Macromolecules* **2000**, *33*, 5918−5931.
(35) Naughton, J. R.; Matsen, M. W. Limitations of the Dilution Approximation for Concentrated Block Copolymer/Solvent Mixtures. *Macromolecules* **2002**, *35*, 5688−5696.

DOI: 10.1021/acsmacrolett.9b00043
ACS Macro Lett. 2019, 8, 261−266